Characteristics of coronal mass ejections associated with long wavelength type II radio bursts

N. Gopalswamy,[1,2] S. Yashiro,[1,2] M. L. Kaiser,[3] R. A. Howard,[4] and J.-L. Bougeret[5]

Abstract

We investigated the characteristics of coronal mass ejections (CMEs) associated with long wavelength type II radio bursts in the near-Sun interplanetary medium. Type II radio bursts in the decameter-hectometric (DH) wavelengths indicate powerful MHD shocks leaving the inner solar corona and entering the interplanetary medium. Almost all of these bursts are associated with wider- and faster-than-average CMEs. A large fraction of these radio-rich CMEs were found to decelerate in the coronagraph field of view, in contrast to the prevailing view that most CMEs display either constant acceleration or constant speed. We found a similar deceleration for the fast CMEs (speed > 900 km s^{-1}) in general. We suggest that the coronal drag could be responsible for the deceleration, based on the result that the deceleration has a quadratic dependence on the CME speed. About 60% of the fast CMEs were not associated with DH type II bursts, suggesting that some additional condition needs to be satisfied to be radio-rich. The average width (66°) of the radio-poor, fast CMEs is much smaller than that (102°) of the radio-rich CMEs, suggesting that the CME width pays an important role. The special characteristics of the radio-rich CMEs suggest that the detection of DH radio bursts may provide a useful tool in identifying the population of geoeffective CMEs.

1. Introduction

Radio observations in the 1-14 MHz frequency band are now possible thanks to the WAVES experiment [Bougeret et al., 1995] onboard the Wind spacecraft [Acuña et al., 1995]. This frequency band corresponds to the Decameter-Hectometric (DH) wavelength domain and bridges the gap between the traditional metric band accessible to ground based radio telescopes and the kilometric band employed by spaceborne radio instruments. Solar radio phenomena observed in this band are primarily the type III bursts (due to electron beams leaving the Sun) and type II bursts (shocks propagating away from the Sun) [Gopalswamy et al., 1998; Kaiser et al., 1998; Reiner and Kaiser, 1999]. Occasionally, type IV bursts from propagating ejecta containing nonthermal particles are observed [Leblanc et al., 2000]. Sometimes storms consisting of a large number of type III bursts in quick succession are also observed. There is also a variant of type III bursts known as shock-associated (SA) events, which seem to be observed in association with DH type II bursts [Cane, et al., 1981; Reiner et al., 2000; Bougeret et al., 1998; Gopalswamy et al., 2000b]. The DH radio observations have confirmed most of the current ideas on nonthermal radio bursts; in addition, they have provided new information towards a better understanding of coronal mass ejections (CMEs) near the Sun [Gopalswamy et al., 2000b].

The DH radio emission originates roughly in the outer corona and IP medium corresponding to a heliocentric distance of about 2-10 $R_\odot$ where the electron density drops from a few times 10^6 to below 10^5 cm^{-3}. The DH band thus corresponds to a region in the corona where the topology of the magnetic field changes from closed to open field configuration. The solar wind starts to pick up speed in this region of the low-latitude corona. Solar ejecta that reach the heights corresponding to the DH domain are likely to leave the Sun forever. The kilometric domain, which corresponds to the IP medium, begins at the long wavelength end of the DH domain. It is well known from the past observations that almost all of the kilometric type II bursts (caused by IP shocks) are associated with CMEs [Cane et al. 1987]. This is expected because almost all of the IP shocks are associated with CMEs [Sheeley et al., 1985]. Since DH type II bursts are also due to shocks, one might ask whether these shocks are also driven by CMEs. Recently, Gopalswamy et al. [2000b] studied a small number of DH type II bursts and found them to be associated with CMEs that were faster and wider on the average. Since type II bursts in the metric domain are not good indicators of IP events [Gopalswamy et al., 1998; 2001], the DH type II burst might serve as proxies for energetic CMEs, likely to be geoeffective. Thus, observing DH type II bursts is one way of identifying geoeffective CMEs if they originate on the front side. For this, we need to know if the CMEs associated with the DH type II bursts have any special characteristics as compared to CMEs in general. In this paper, we perform a statistical analysis of a large number of such radio-rich CMEs observed by the Solar and Heliospheric Observatory (SOHO) using its Large Angle and Spectrometric Coronagraph (LASCO) [Bruekner et al., 1995]. Specifically, we study the speed, width, and acceleration of CMEs associated with DH type II bursts, and compare them with those of all CMEs.

2. Data Selection

The WAVES experiment on board the Wind spacecraft began observations in November 1994. Although there were several type II

bursts in the kilometric (< 1 MHz) domain from the beginning, the DH (1-14 MHz) type II bursts started only in April 1997. The SOHO observations began in January 1996. Thus SOHO and Wind have overlapping observations for more than five years, from the minimum to maximum of solar cycle 23. It is important to note that the two spacecraft probe roughly the same region of the solar atmosphere. The type II radio bursts are thought to be produced by shock-accelerated electrons at the fundamental and harmonic of the local plasma frequency. The DH spectral domain corresponds to plasma frequencies within the field of view of the SOHO/LASCO coronagraphs. Thus, by measuring the heliocentric distance of the white-light CME, it is possible to infer the heliocentric distance of the DH type II bursts originate. The primary criterion we used to select the events is that there must be a type II radio burst occurring at any frequency between 14 and 1 MHz, irrespective of whether there is any burst in the metric or kilometric domains. In all, there were 138 distinct DH type II bursts during the study period. A few of the events were classified as type IV bursts, but the presence of a type II burst could not be ruled out in these cases, so we included them. There was an extended data gap for about three months (July-September 1998) when SOHO was temporarily disabled. In addition to this major data gap, there were occasional minor data gaps. Since we are interested in the properties of white-light CMEs associated with DH type II bursts, we dropped those type II bursts which occurred during the SOHO data gaps from our analysis. These considerations resulted in a list of 103 DH type II bursts with SOHO/LASCO observations. We were able to identify a unique white-light CME for each one of these DH type II bursts, except for two events. The DH type II burst of November

7, 1998 at 00:20 UT probably originated from the northwest quadrant, from where a number flares occurred on November 06. Although there was a gradual C-level GOES flare, it was not listed in the Solar Geophysical Data. There were two west-limb CMEs in the appropriate time window so the identification is ambiguous. The other DH type II burst on December 16, 2000 probably originated from the backside and it was not possible to detect the associated CME. For two other DH type II bursts, we were able to identify the corresponding white-light CMEs, but the solar energetic particles from the preceding CMEs (July 14, 2000 and November 8, 2000 events) swamped the SOHO detectors and hence we were not able to make useful measurements on these CMEs. The remaining 101 DH type II bursts and the corresponding white-light CMEs are listed in Table 1. For convenience, we refer to these radio-rich CMEs as "DH CMEs".

Figure 1 shows the WAVES dynamic spectrum of the DH type II burst of October 25, 2000. The type II burst is the slanted streak starting around 10:00 UT near 10 MHz and drifting to lower frequencies. The intense vertical feature is the type III-like burst (SA event). The type II burst has a weaker fundamental component, which is not as continuous as the harmonic component. This is common in limb events because the fundamental is usually absorbed by the overlying corona. Figure 1(b) shows the corresponding white-light CME at two instances. When the type II radio emission is at 3 MHz, the local plasma frequency is 1.5 MHz (because of harmonic emission) and hence the electron density is 2.8×10^4 cm^{-3}. This density must prevail at a heliocentric distance of about 10 R_s because the white light CME is at this distance around 11:42 UT. The shock front is

expected to be very close to the leading edge of the CME. The radio emission continues to lower frequencies beyond the field of view of the LASCO coronagraph. There was no metric type II burst associated with this event. The CME was accelerating at a rate of 17 m s^{-2} and might have had a very small speed in the inner corona (see the height-time plot in Fig. 1c). The source region was a filament eruption from N15 W75. It must be pointed out that not all type II bursts are as spectacular as the October 25, 2000 event.

Columns 2 and 3 of Table 1 give the date and universal time (UT) of the DH type II radio bursts. The time of first appearance of the corresponding white-light CME in the field of view of the LASCO/C2 coronagraph is given in column 4 as the "CME time." Note that the actual lift-off time of the CME is earlier than this time. The central position angle (PA) of the CME is given in column 5. There is no central position angle for halo CMEs, so these are denoted by "Halo" in column 5. The position-angle extent of the CMEs in the sky plane defines their width and is listed in column 6. It is very difficult to relate the measured width to the physical size of the CME. For example, the width of halo CMEs is listed as 360° because the CME appears to surround the occulting disk of the coronagraph [see, e.g., Howard et al., 1982]. In column 6, some of the entries are prefixed with a > symbol. These CMEs have a bright main part and a diffuse extended part, making them appear as halo CMEs later on. The diffuse part may be the white-light manifestation of the CME-driven shock.

The speed is one of the primary characteristics of a CME, which is obtained from the height-time measurements. The speed was obtained from both linear (constant speed) and quadratic (constant acceleration) fits to the height-time measurements. The linear fit gives the average speed (V_1). From the quadratic fit, we obtained the initial (V_{2i}) and final (V_{2f}) speeds corresponding to the times of first and last measurements within the coronagraph field of view, respectively. All the speeds correspond to the sky plane, roughly at the central position angle of the CME. No attempt was made to correct for the projection effects. For halo CMEs the measured speed corresponds to the position angle of maximum speed. The three speeds are listed in columns 7-8 in Table 1. The acceleration (m s^{-2}) of the CMEs, obtained from the quadratic fit to the height-time measurements, is listed in column 10. In the last column, we have given the source location of the CMEs. The source location is the heliographic coordinates of the general region of eruption. For example, S25E16 for event # 1 means that the eruption occurred at 25°S and 16°E. In most cases, the location corresponds to the position of the associated H-alpha flare obtained from the Solar Geophysical Data as listed in the NOAA web site. In addition, we confirmed the source positions using a number of different data sets: (1) The daily movies of EUV images obtained by the Extreme-ultraviolet Imaging Telescope (EIT) [Delaboudinière, 1995]; these movies are made 195 Å images obtained with a cadence of ∼ 12 min and help identify the eruptions as a dimming, arcade formation or filament/prominence eruption [see, e. g., Gopalswamy, 1999]. (2) The daily movies of full disk X-ray images obtained by the soft X-ray telescope (SXT) [Tsuneta et al., 1991] on board the Yohkoh mission. These movies can identify faint, large-scale post eruption arcades over a large temperature range. When only a post-eruption arcade is observed, the eruption location is given as the geometrical center of the arcade. (3) The daily movies

made from the microwave images obtained by the Nobeyama radioheliograph [Nakajima, et al. 1994] to identify the prominence or filament eruptions wherever possible. (4) Images in the SOHO archive obtained by space and ground based instruments were helpful in confirming the source locations of some events.

The source location is also used to decide whether the associated CME is a disk or limb event. In the preliminary study using a subset of 27 DH radio bursts, Gopalswamy et al. [2000b] found a positive correlation between central meridian distance of the solar source and the associated CME speed suggesting strong projection effects. In order to obtain CME properties free from projection effects, we also analyzed a subset of DH type II bursts associated with limb CMEs. When the solar source of the CME is at a central meridian distance (CMD) $> 60°$ the type II burst is considered as a limb event. The limb events are denoted by an asterisk in Table 1. Note that some of the limb events are listed without the latitude (e.g., NE90 or W90). This means the events occurred behind the limb, but probably not too far. Typically CMEs occurring within 30° from the limb are considered as limb events. It is possible that some of the limb events might have occurred more than 30° behind the limb. Source regions of backside halo events are listed as "Backside" in column 11 of Table 1. There were 39 limb events in all, 4 backside events and the remaining were disk events. While presenting the statistical properties, we consider three populations of CMEs: (i) all DH CMEs, (ii) limb DH CMEs (a subset of (i)) and (iii) the general population of CMEs.

3. Statistical Analysis and Results

It is customary to characterize the white-light CMEs using their speed, angular width in the sky-plane, and the central position angle. In this study we include the acceleration of CMEs as an important property. The speed is obtained by fitting a straight line or a second order polynomial to the measured height-time data points. For the purpose of characterizing the speed of CMEs, we only use the straight line fit. This means, for CMEs with significant acceleration, the characteristic speed is an average value within the LASCO field of view.

3.1. Speed of DH CMEs

Figure 2 shows the distribution of the speeds of the 101 DH CMEs listed in Table 1. The speeds were in the range 241 to 2519 km s^{-1}, with an average of 961 km s^{-1}. This average is about twice the average speed (487 km s^{-1}) of the nearly 3000 LASCO CMEs observed between January 1996 and December 2000 [St. Cyr et al., 2000; Yashiro et al., 2001]. Most of the DH CMEs had speeds greater than the average speed of all CMEs. In fact only 17 events ($\sim$17%) had speeds less than this average value. For the limb-DH CMEs, the speed range was 356 to 2221 km s^{-1}, with an average of 1144 km s^{-1}. The average value for the limb events is larger because the speed measurements have minimal projection effect. This is clearly seen from the fact that the two lowest speed bins disappeared for the limb events. Note also that only four out of the 39 limb-DH CMEs ($\sim$10%) had speed less than the average speed of all CMEs.

3.2. Width of DH CMEs

Table 1 shows that more than half of the DH CMEs (53/101) were halo CMEs. Even among the limb events, 17 were halo CMEs (44%). This already points to the large size of the DH CMEs or rapid expansion early on. Excluding DH CMEs with width > 200° as halo events, we found that the remaining 45 DH CMEs had widths in the range 25° to 190°, with an average value of 102°. This is again much larger than the average width (58°) of all non-halo LASCO CMEs. The width of non-halo limb-DH events had an average of 112°. Figure 3 shows the distribution of DH-CME widths. Note that more than 95% of the DH CMEs had widths exceeding the average width of all CMEs. Combined with the fact that most of the DH CMEs are faster than average, we infer that they are more energetic.

There is also a weak correlation between the width and speed of the DH CMEs. Figure 4 shows the speed-width scatter plots for all DH events (top) and limb events (bottom). Since we do not know the actual width of halo CMEs, we restricted to events with width < 200°. While the limb events show a weak correlation (correlation coefficient r = 0.56), the correlation is somewhat poorer (r = 0.44) for all DH CMEs considered as a class.

3.3. Acceleration of DH CMEs

It is generally believed that CMEs either accelerate or have constant speed within the coronagraphic field of view [MacQueen and Fisher, 1983; Sheeley et al., 1999]. Sheeley et al. [1999] measured the speeds of slow and fast halo CMEs and came to the same conclusion. They found that fast CMEs, when observed broadside, invariably moved with constant speed, while fast halos decelerated.

Since halo events in the LASCO/C3 field of view are expected to be located much farther than they appear [see Michels et al., 1997], Sheeley et al.'s result implies that the fast halos decelerate at distances beyond 30 R_s. However, decelerations were found even for broadside (limb) events in individual cases [Wood et al., 1999]. Figure 5 shows three distinct height-time profiles chosen from the list of DH CMEs in Table 1. Straight-line fit (constant-speed) is definitely not possible for all of them. Quadratic fit (constant acceleration or deceleration) is better suited for cases (a) and (c), while straight-line fit seems to be reasonable for case (b). We determined the acceleration of the DH CMEs by fitting a second order polynomial to the height-time measurements obtained from C2 and C3 images. The distribution of accelerations is shown in Figure 6. We restricted to events with the number of data points ≥ 4 so that the derived acceleration is reliable (see Table 1). A surprising result is that there is a clear tendency for a majority (60%) of the DH CMEs to slow down within the C3 field of view (30 $R_\odot$). There is an extended tail on the deceleration side of the distribution for both limb and non-limb of DH CMEs. In fact the average acceleration of limb CMEs is -11.3 m s^{-2}, compared to an average of -6.4 m s^{-2} for all the DH CMEs. These results are in contradiction to the traditional view that CMEs show constant acceleration or constant speed. While there are many events in the central bin (-5 to 5 m s^{-2}), which may correspond to constant speed, half of the limb DH events have deceleration < - 15 m s^{-2}.

3.4. Relationship between CME speed and deceleration

The propelling force of the CMEs is probably still active in the coronagraph field of view

for the accelerating events, while it might have weakened considerably for the decelerating events. In order to study the relationship between acceleration and speed, we considered the population of decelerating DH CMEs. Table 1 shows that there were 61 decelerating events. As before, we considered only those CMEs for which there were at least four measurements. Figure 7 is a scatter plot of the acceleration and speed. The acceleration is clearly anticorrelated with the speed, suggesting that faster events decelerate more. The correlation coefficient is - 0.76 for all DH CMEs and -0.83 for limb-DH CMEs. We have also shown the linear and quadratic fits to the data points. The quadratic fit seems to represent the data better.

The deceleration of the CMEs can be explained if we consider all the forces acting on the CMEs: The propelling force, gravity, and drag [see, e.g., Chen, 1997]. The propelling force is the sum of all outward forces. The coronal drag (F_d) is given by,

$$F_d = C_d \rho A (V_{sw} - V_{CME}) |V_{sw} - V_{CME}|, \quad (1)$$

where C_d is the drag coefficient, ρ is the ambient coronal density, A is the characteristic surface area of the CME, V_{sw} is the solar wind speed, and V_{CME} is the CME speed. MHD simulations suggest that the drag coefficient C_d is of order unity [see, e.g., Cargill et al., 1996]. Since we are dealing with fast CMEs, $V_{sw} < V_{CME}$ and the drag is always a retarding force for fast CMEs. In the inner corona, the solar wind is still accelerating, so the drag force is approximately quadratic in the CME speed, in agreement with our observations. Wider CMEs present a larger surface area and hence are subject to more drag force.

If the above explanation for the CME deceleration is correct, then all fast CMEs must decelerate. To see this, we determined the acceleration of all fast CMEs ($V_{CME} > 900$ km s^{-1}) that occurred during January 1996 to December 2000. We chose 900 km s^{-1} because it is close to the average speed of the DH CMEs (see, Fig. 2). There were 262 fast CMEs in all. The resulting distribution of acceleration is shown at the bottom of Figure 6 along with that for the DH CMEs. There is a clear skew of the distribution towards the negative side of the acceleration and the peak of the distribution is around -20 m s^{-2}. Thus, we conclude that the DH CMEs show significant deceleration primarily because they are faster and wider than average, and hence interact strongly with the coronal medium.

4. Discussion and Conclusions

The primary finding of this study is that the CMEs associated with DH events are faster and wider on the average, confirming the preliminary results of Gopalswamy et al. [2000b]. This in turn implies that CMEs capable of driving shocks in the IP medium are very energetic. We note that only about 40% of the fast ($V_{CME} > 900$ km s^{-1}) are associated with DH type II bursts; the remaining 60% are radio-poor. Production of type II bursts depends on additional factors such as the conditions for shock formation, the ability of the shock to accelerate nonthermal electrons and so on. A quick look at the population of fast radio-poor CMEs revealed that they are not as wide as the radio-rich events. Figure 8 is a histogram of the widths of the radio-poor CMEs (as before, we excluded CMEs with widths > 200°). Note that there is a huge population of narrow CMEs in the distribution. The average width (66°) of the radio-poor CMEs is much smaller than that (102°) of the radio-rich CMEs. Thus the width of the CMEs seems to be an impor-

tant factor in deciding whether a fast CME is capable of producing long-wavelength radio emission. We are investigating the radio dynamic spectra corresponding to the fast CMEs without DH type II bursts and the results will be published elsewhere. The second result is the tendency for the wider DH CMEs to be faster. In addition, we found a surprising result that the DH CMEs show a pronounced deceleration within the LASCO/C3 field of view. This result may have important implications to understand the evolution of CMEs in the IP medium by the combined action of propelling and retarding forces. The drag force of the ambient corona acting on the CMEs is significant near the Sun because of the high density and low solar wind speed.

The fact that all the DH type II bursts are associated with CMEs implies that CMEs drive powerful IP shocks in the IP medium. Sheeley et al. [1985] had investigated the properties of white-light CMEs associated with IP shocks. The CMEs in Sheeley et al. [1985] were observed by the Solwind Coronagraph on board the P78-1 satellite while the associated IP shocks were detected in situ by the Helios-1 spacecraft. The data used in that study were obtained when the two spacecraft were in quadrature so the projection effects were minimal. It is therefore instructive to compare our results from the limb events with those of Sheeley et al. [1985]. The speed and width of the shock-associated CMEs obtained by Sheeley et al. were above-average, as in our case. For non-halo events, they found an average width of 88°, slightly lower than our average for non-halo limb events. Similarly the average speed of Sheeley et al. was 749 km s^{-1} compare to our 1144 km s^{-1}. The difference in the average speeds can be explained by the fact that some CMEs continue to accelerate and produce shocks in the IP

medium without producing type II bursts in the DH domain; these CMEs would not have been included in our study. The large number of kilometric type II bursts without metric or DH type II bursts observed by Wind/WAVES [Gopalswamy et al. 2001] support this explanation. In the list published in Sheeley et al. [1985], 20 shocks were followed by pistons. For this population, the CME-shock association is expected to be unambiguous. For these 20 events, the average width of the associated CMEs is 96°, much closer to our result. Speed measurements were available only for 15 of the 20 events, yielding an average CME speed of 944 km s^{-1}, again closer to our result.

Our result on the deceleration of fast CMEs, however, does not agree with Sheeley et al.'s result that "none of the fast ones decelerated by a significant amount." We have shown that a major fraction of all fast CMEs (which obviously include DH CMEs) decelerate. One reason for this discrepancy may be the smaller field of view (2.5 - 10 R_s) of the Solwind coronagraph (compared to LASCO's 30 R_s), which makes it difficult to measure deceleration. Even with LASCO data, Sheeley et al. [1999] concluded that impulsive CMEs, when viewed broadside, appear to "move uniformly across the 2-30 R_s field of view with speeds typically in excess of 750 km s^{-1}." They illustrated this point with only one example, the April 14, 1998 event. However, there seems to be a slight problem with their plot: they had used only LASCO/C3 data and hence missed the two initial points from LASCO/C2 data. When these two points are included, the height-time data fit to a quadratic curve, with a constant acceleration of ~28 m s^{-2} at PA 58° and ~18 m s^{-2} at PA 82°. Thus, the range of heights over which the CME is measured is an important factor in deciding the acceleration [Gopalswamy and Thomp-

son, 2000].

To conclude, this study suggests that the DH type II bursts are indicators of faster and wider CMEs, thus providing a useful means of identifying those solar eruptions that are likely to reach 1 AU. To be geoeffective, the CME has to first arrive at Earth and should contain magnetic field with southward component. Gopalswamy et al. [2000a] showed that the CMEs which arrived at the Earth originated from close to disk center (average distance in latitude and longitude of $17°$ and $28°$, respectively). Since the DH type II bursts originate from all longitudes on the disk as well as from behind the limb, we need to combine radio observations with those at other wavelengths such as optical, X-ray, microwave or EUV to identify the location of eruption. The limb DH type II events, on the other hand, are useful in obtaining the actual characteristics of CMEs, free from projection effects.

References

Acuña, M. H., et al., The global geospace program and its investigations, *Space Sci. Rev.*, *71*, 5, 1995.

Bougeret, J.-L. et al., Waves: The Radio and Plasma Wave Investigation on the Wind Spacecraft, *Space Sci. Rev.*, *71*, 231, 1995

Bougeret, J.-L. et al., A shock associated (SA) radio event and related phenomena observed from the base of the solar corona to 1 AU, Geophys. Res. Lett., 25, 2513, 1998.

Brueckner, G.E., et al., The large angle spectroscopic coronagraph (LASCO), *Sol. Phys.*, *162*, 357, 1995.

Cane, H. V. et al., Radio evidence for shock accelerated electrons in the Solar corona, *Geophys. Res. Lett.*, *8*, 1285, 1981.

Cane, H. V., N. R. Sheeley, and R. A. Howard, Energetic interplanetary shocks, radio emission, and coronal mass ejections, *J. Geophys. Res.*, *92*, 9869, 1987.

Cargill, P. J., J. Chen, D. S. Spicer, and S. T. Zalesak, Magnetohydrodynamic simulations of the motion of magnetic flux tubes through a magnetized plasma, *J. Geophys. Res.*, *101*, 4855, 1996.

Chen, J., Coronal mass ejections: causes and consequences, A theoretical view, in *Coronal Mass Ejections*, edited by N. Crooker, J. A. Joselyn, and J. Feynman, (Geophys. Monogr. 99; Washington DC: AGU), p. 65, 1997.

Delaboudinière, J. P., et al., EIT: extreme-ultraviolet imaging telescope for the SOHO Mission, *Sol. Phys.*, *162*, 291, 1995.

Gopalswamy, N., X-ray and microwave signatures of a coronal mass ejections, in *Solar Physics With Radio Observations*, edited by T. Bastian, N. Gopalswamy, and K. Shibasaki, *Rep. 479*, Nobeyama Radio Obs., Nobeyama, Japan, 1999.

Gopalswamy, N., M. L. Kaiser, R. P. Lepping, S. W. Kahler, K. Ogilvie, D. Berdichevsky, T. Kondo, T. Isobe, and M. Akioka, Origin of coronal and interplanetary shocks: A new look with Wind spacecraft data, *J. Geophys. Res.*,

103, 307, 1998.

Gopalswamy, N., A. Lara, R. P. Lepping, M. L. Kaiser, D. Berdichevsky, and O. C. St. Cyr, Interplanetary acceleration of coronal mass ejections, *Geophys. Res. Lett.*, *27*, 145, 2000a.

Gopalswamy, N., M. L. Kaiser, B. J. Thompson, L. Burlaga, A. Szabo, A. Lara, A. Vourlidas, S. Yashiro, and J.-L. Bougeret, Radio-rich solar eruptive events, *Geophys. Res. Lett.*, *27*, 1427, 2000b.

Gopalswamy, N., A. Lara, M. L. Kaiser, and J.-L. Bougeret, Near-sun and near-Earth manifestations of solar eruptions, *J. Geophys. Res.*, in press, 2001.

Gopalswamy, N. and B. J. Thompson, Early life of coronal mass ejections, *J. Atmos. Sol. terr. Phys.*, *62*, 1457, 2000.

Howard, R. A., D. J. Michels, N. R. Sheeley, and M. J. Koomen, The observations of a coronal transient directed at Earth, *Astrophys. J.*, *263*, L101, 1982.

Kaiser, M. L. et al., Type II radio emissions in the frequency range 1-14 MHz associated with the April 07, 1997 solar event, *Geophys. Res. Lett.*, *25*, 2501, 1998.

Leblanc, Y. G. A. Dulk, I. H. Cairns, and J.-L. Bougeret, Type II fixed on boards flare continuum in the corona and solar wind, *J. Geophys. Res.*, *105*, 18215, 2000.

MacQueen, R. M. and R. Fisher, The kinematics of solar inner coronal transients, *Solar Phys.*, *89*, 89, 1983.

Michels, D. J., R. A. Howard, M. J. Koomen, S. Plunkett, G. E. Brueckner, P. Lamy, R. Schwenn, and D. A. Biesecker, Visibility of Earth-directed Coronal Mass Ejections, in Proc. of Fifth SOHO Workshop, ESA SP 404, p. 567, 1997.

Nakajima, H., et al., The Nobeyama radioheliograph, *Proc. IEEE, 82*, 705, 1994.

Reiner, M. J. and Kaiser, M. L., High frequency radio emissions associated with shocks driven by coronal mass ejections, *J. Geophys. Res.*, *104*, 16979, 1999.

Reiner, M. J., M. Karlický, K. Jiřička, H. Aurass, G. Mann, and M. L. Kaiser, On the solar origin of complex type III-like radio bursts observed at and below 1 MHz, *Astrophys. J.*, *510*, 1049, 2000.

Sheeley, N. R., Jr., R. A. Howard, M. J. Koomen, D. J. Michels, R. Schwenn, K. H. Mulhauser, and H. Rosenbauser, Coronal mass ejections and interplanetary shocks, *J. Geophys. Res.*, *90*, 163, 1985.

Sheeley, N. R., Jr., J. H. Walters, Y.-M. Wang, and R. A. Howard, Continuous tracking of coronal outflows: Two kinds of coronal mass ejections, *J. Geophys. Res.*, *104*, 24,739, 1999.

St. Cyr, O.C. et al., Properties of coronal mass ejections: SOHO LASCO observations from January 1996 to June 1998, *J. Geophys. Res.*, *105*, 18,169, 2000.

Tsuneta, S., L. Acton, M. Bruner, J. Lemen, W. Brown, R. Caravalho, R. Catura, S. Freeland, B. Jurcevich, and J. Owens, The soft X-ray telescope for the SOLAR-A mission, *Solar Phys.*, *136*, 37, 1991.

Wood, B. E. M. Karovska, J. Chen, G. E. Brueckner, J. W. Cook, J. W., R. A. Howard, Comparison of Two Coronal Mass Ejections Observed by EIT and LASCO with a Model of an Erupting Magnetic Flux Rope, *Astrophys. J.*, *512*, 484, 1999.

Yashiro, S., N. Gopalswamy, G. Michalek, O. C. St. Cyr, and R. A. Howard, A comprehensive catalog of SOHO/LASCO coronal mass ejections, under preparation, 2001.

N. Gopalswamy, M. L. Kaiser and S. Yashiro, NASA GSFC, Building 26 Room G1, Mail code 682.3, Greenbelt, MD 20771. (gopals@fugee.gsfc.nas

A. Lara, Institute Geofisica, UNAM, Mexico City, Mexico

R. A. Howard, Naval Research Laboratory, Washington, D. C.

J.-L. Bougeret, Observatoire de Paris, 5 Place Jules Janssen, Meudon, France.

[1]Center for Solar Physics and Space Weather, The

Catholic University of America, Washington DC

[2]Also at NASA Goddard Space Flight Center, Greenbelt, Maryland

[3]Code 695.0, NASA Goddard Space Flight Center, Greenbelt, Maryland

[5]Naval Research Laboratory, Washington DC
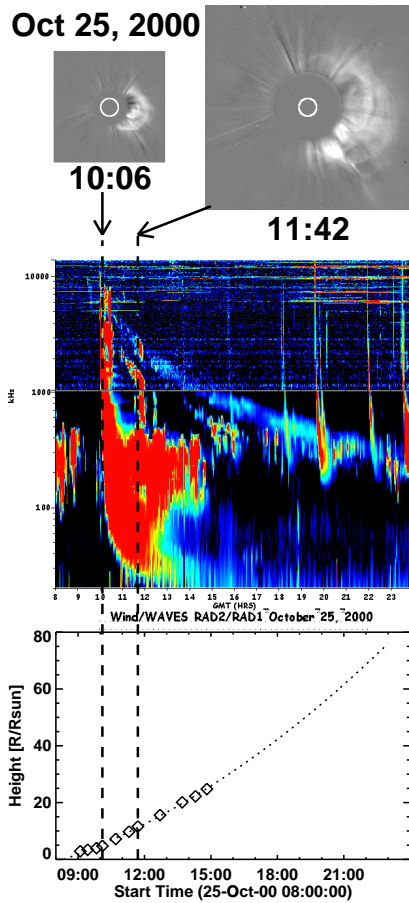
Figure 1. The October, 25, 2000 CME and the associated type DH II burst. The vertical feature in the radio dynamic spectrum is the type III-like burst, also known as SA event. The continuous slanted feature is the harmonic component of the type II burst, while the intermittent slanted feature is the fundamental component. At the top LASCO images of the CME are shown at two instances, one close to the onset of the type II burst (10:06 UT) and the other at 11:42 UT. The corresponding times are also marked on the radio dynamic spectrum by the two vertical dashed lines. The height-time plot of the CME are shown at the bottom. The diamonds represent the measured height-time data. A quadratic fit to these data points is shown by the dotted line, extrapolated to the time range of the type II burst.
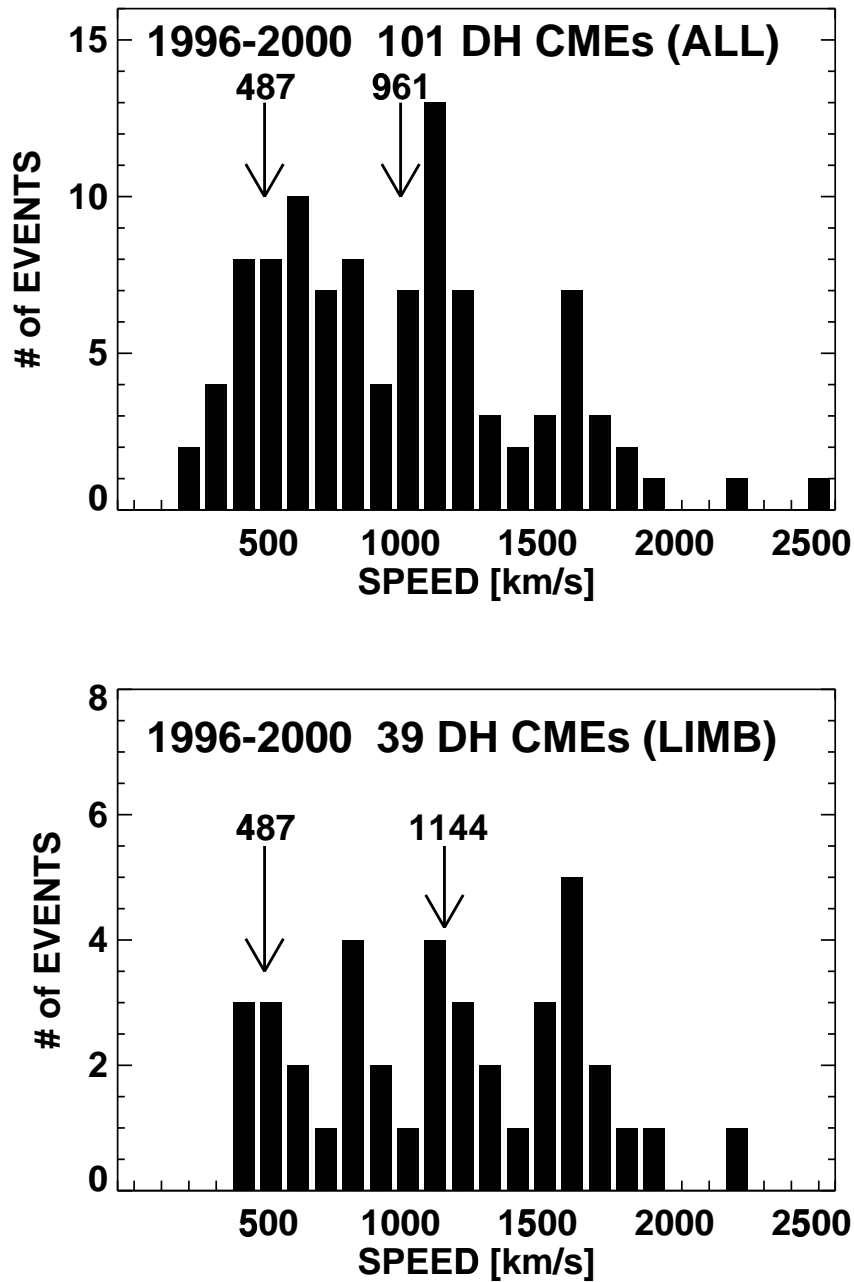
Figure 2. Histogram showing the speed distribution of all DH CMEs (top) and for the DH CMEs originating from near the limb (bottom). The average speeds of all CMEs (487 km s^{-1}) and the DH CMEs (961 km s^{-1} for all DH CMEs and 1144 km s^{-1} for limb DH CMEs) are indicated by arrows.
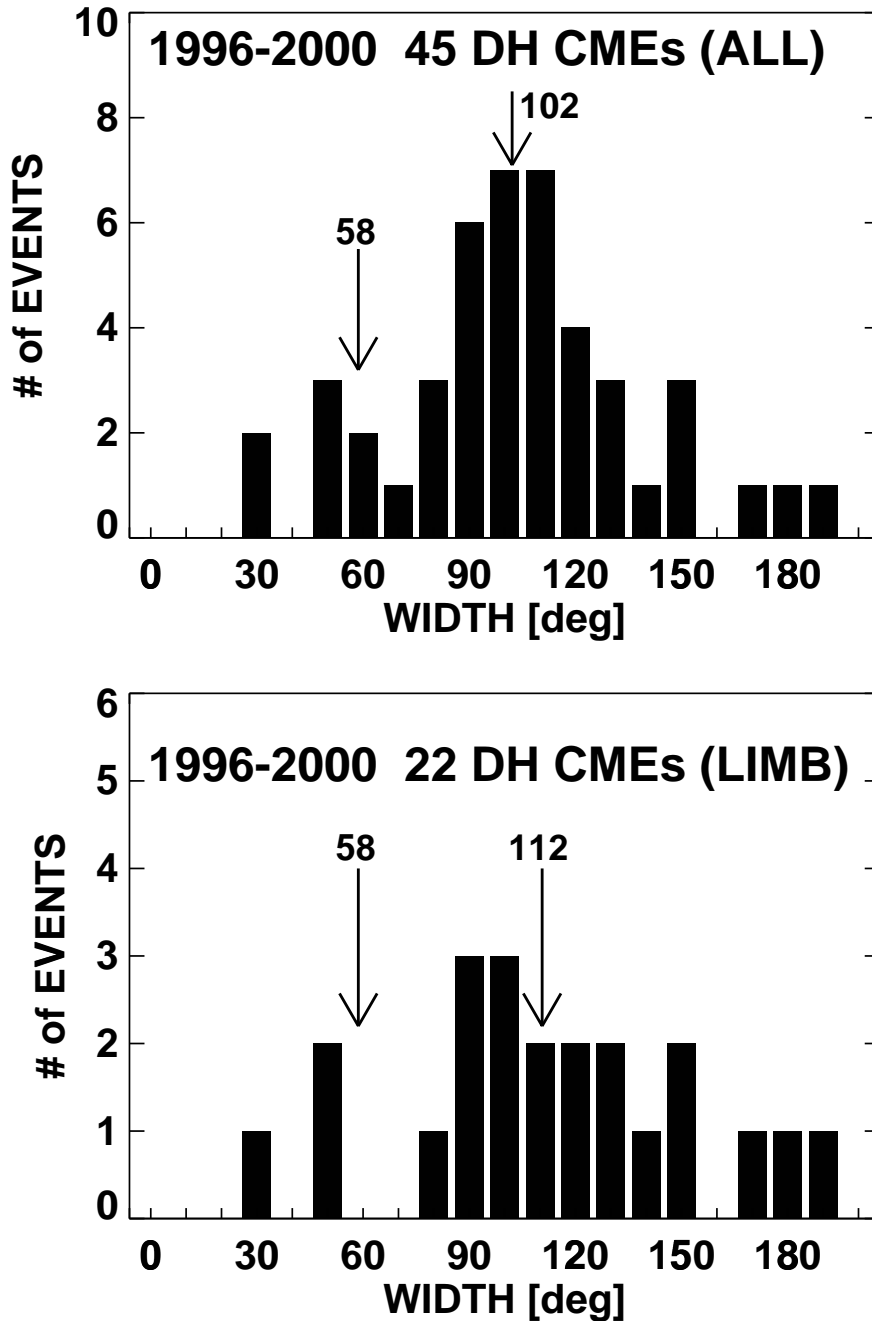
Figure 3. Histograms showing the distribution of DH-CME widths. As before we have shown the distribution for all the DH CMEs (top) and for limb events (bottom). We have excluded the full halo events (width > 200°) from the histograms. The average width of the general population of CMEs (58°) and of the DH CMEs (102° for all and 112° for limb events) are indicated by arrows.
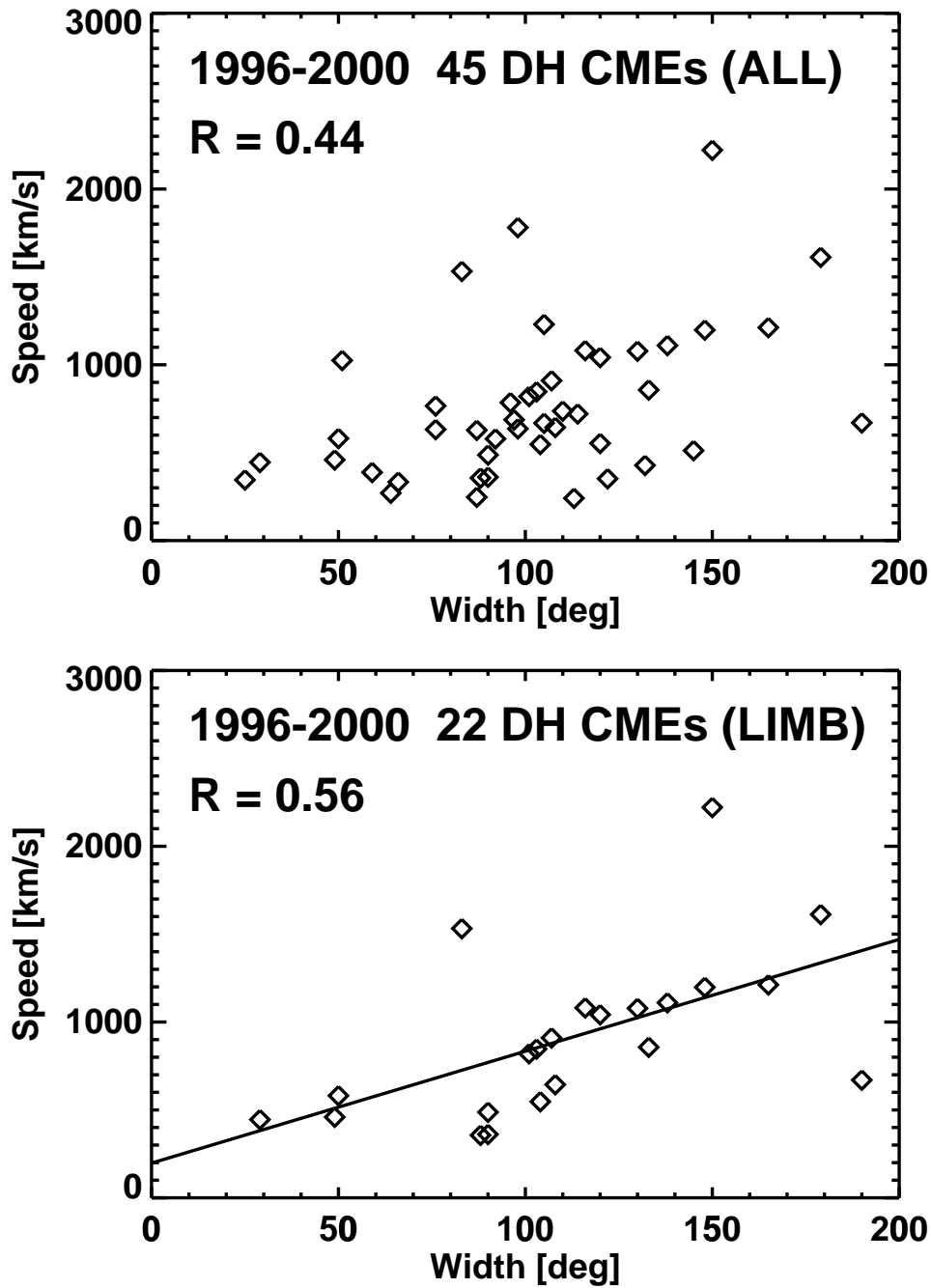
Figure 4. The speed-width scatter plots for all DH events (top) and limb events (bottom). In the bottom plot, a straight line fit to the data points is also shown. The correlation coefficients (R) are also given on the plots. The speed used is the first order speed (V_1 in Table 1). As in Fig. 3, only those events with width < 200° are included.
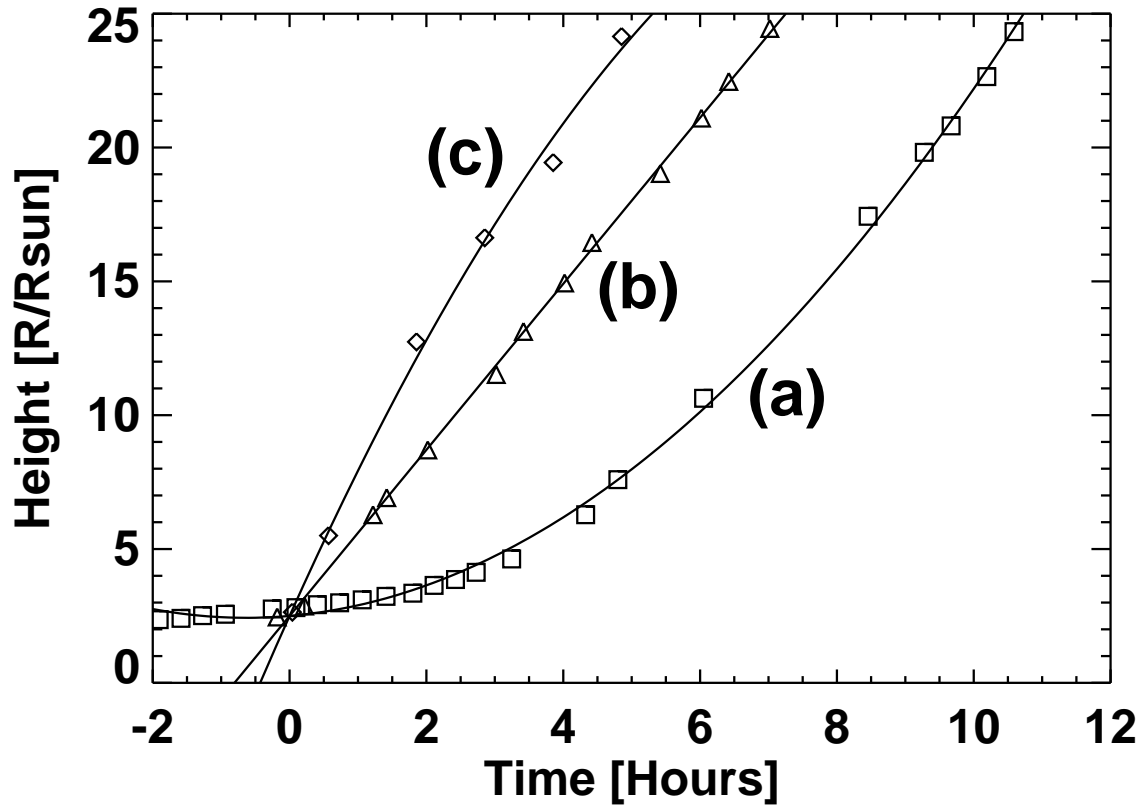
Figure 5. Three distinct height-time profiles found in our sample of events: (a) the accelerating CME of June 21, 1998 at 18:15 UT, (b) the constant-speed CME of February 17, 2000 at 20:06 UT, and (c) the decelerating CME of May 11, 1998 at 21:55 UT. The solid lines are the fits to the data points. On the X-axis, zero corresponds to the time when each CME reached a height of 2.5 R_s. Properties of the CMEs are listed in Table 1.
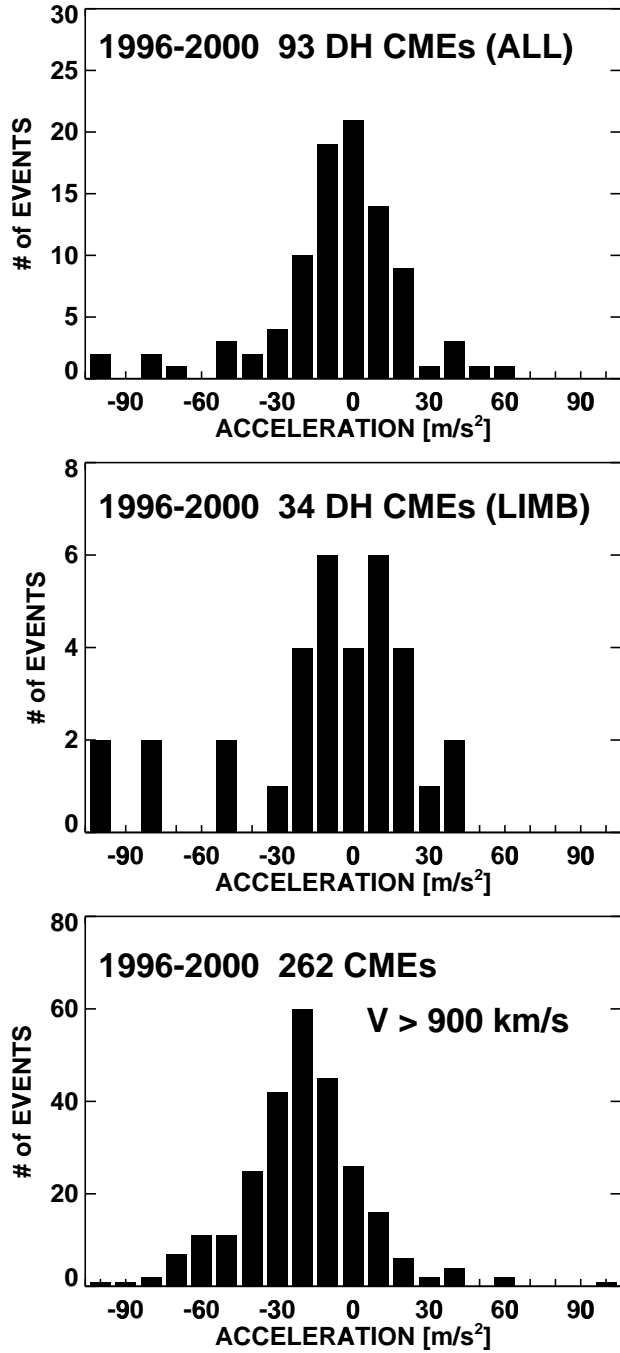
Figure 6. Histograms showing the distribution of accelerations for all DH CMEs (top), for limb DH events (middle), and for all fast (speed > 900 km s^{-1}) CMEs (bottom). The range of accelerations is restricted to ± 100 m s^{-2}. We have included only those events with at least 4 height-time measurements.
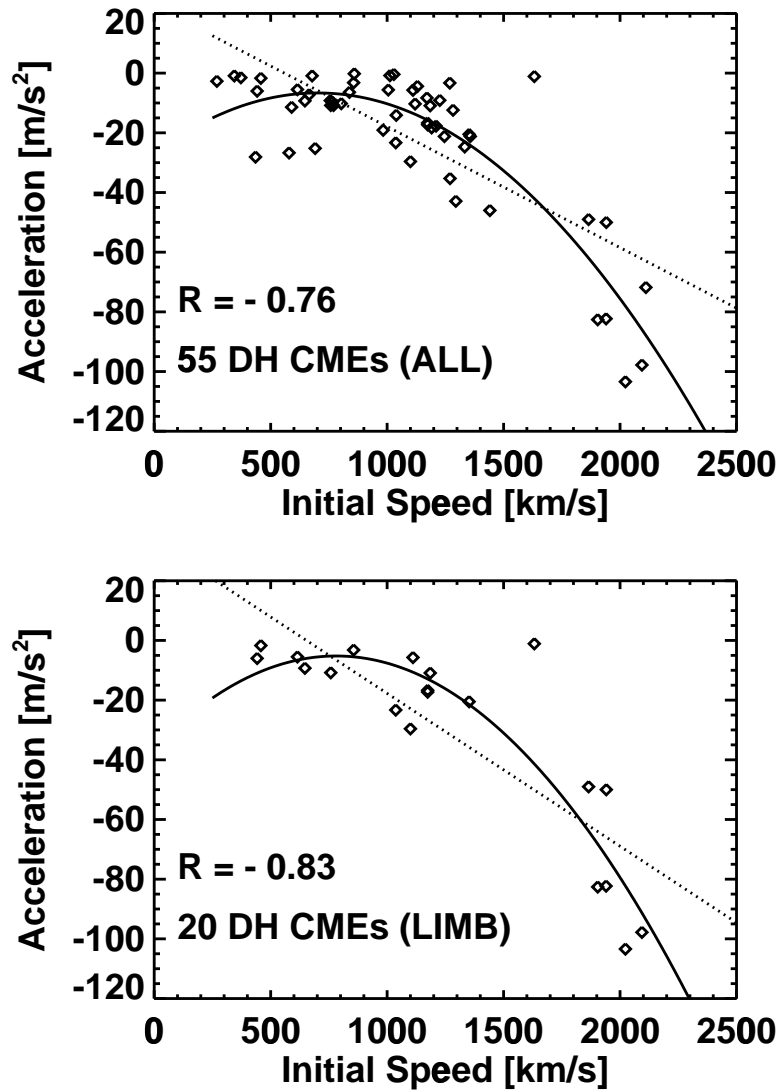
Figure 7. Scatter plots showing the relation between acceleration and initial speed for all DH CMEs (top) and limb events (bottom). We have included only those events with deceleration (acceleration < 0), and have excluded the events that have only 3 data points. The correlation coefficients (R) along with the linear (dotted line) and quadratic (solid curve) fits to the data points are also shown.
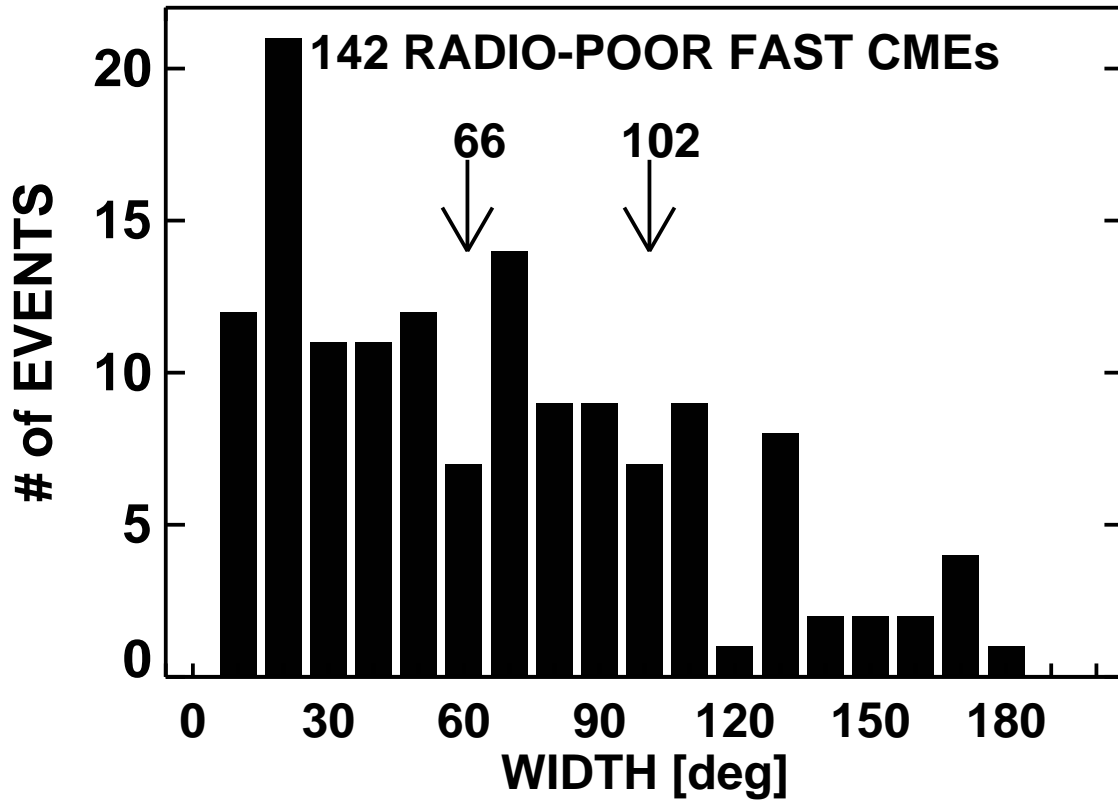
Figure 8. Histogram of the widths of the fast CMEs (speed > 900 km s^{-1}) observed between 1996 and 2000. The average of the distribution is 66° as marked. The average width (102°) of radio-rich CMEs is also marked for comparison. We excluded halo CMEs (width > 200°).

Table 1. Characteristics of CMEs associated with DH type II Bursts

| Number	Radio Date	Time	CME Time	PA	Width	$V1$	$V2_i$	$V2_f$	Accel	Location
1	1997/04/01	14:00	14:46	77	066	333	344	322	-0.9	S25E16
2	1997/04/07	14:30	14:27	Halo	360	858	859	856	-0.2	S30E19
3	1997/05/12	04:56	05:50	Halo	360	499	590	409	-11.4	N21W08
4	1997/09/23	21:53	22:02	106	097	687	596	771	8.9	S28E23
5	1997/11/03	05:15	05:28	235	113	241	231	250	1.4	S20W13
6	1997/11/03	10:30	11:11	233	122	352	372	331	-1.5	S20W15
7	1997/11/04	06:00	06:10	Halo	360	789	983	582	-19.1	S14W33
8	1997/11/06	12:10	12:10	Halo	360	1514	1904	1113	-82.6	S18W63*
9	1997/11/27	13:30	11:55	91	088	356	442	271	-6.0	N16E63*
10	1997/12/12	22:45	22:27	281	064	270	260	280	0.6	N25W52
11	1998/01/25	15:03	15:26	Halo	360	570	543	598	2.8	N24E27
12	1998/03/29	03:05	03:48	Halo	360	1397	1416	1378	-4.9^a	SW90*
13	1998/04/20	10:25	10:07	Halo	360	1641	1865	1417	-49.0	S43W90*
14	1998/04/23	05:50	05:27	Halo	360	1596	2094	1104	-97.8	S19E90*
15	1998/04/27	09:20	08:56	Halo	360	1039	1120	951	-10.3	S16E50
16	1998/04/29	16:30	16:58	Halo	360	1074	1210	935	-17.7	S18E20
17	1998/05/02	14:25	14:06	Halo	360	979	1005	954	-5.6	S15W15
18	1998/05/03	22:10	22:02	Halo	360	669	678	659	-0.9	S13W34
19	1998/05/06	08:15	08:04	279	120	1042	989	1100	7.0	S11W65*
20	1998/05/09	03:35	03:35	Halo	360	1920	2642	1252	-166.9^a	S11W90*
21	1998/05/11	21:35	21:55	Halo	360	848	1100	569	-29.6	N32W90*
22	1998/05/19	10:00	10:02	286	096	785	838	729	-6.4	N29W46
23	1998/05/27	13:30	13:45	266	107	910	852	969	6.4	N19W66*
24	1998/06/11	10:15	10:28	96	130	1078	1111	1043	-5.7	N08E90*
25	1998/06/16	18:20	18:27	283	179	1612	1940	1279	-82.3	S17W90*
26	1998/06/20	21:10	18:20	Halo	360	927	1039	799	-14.1	Backside
27	1998/06/22	07:15	$18:15^p$	294	090	361	0	797	18.8	N25W90*
28	1998/11/02	14:00	13:18	104	>145	512	473	552	4.1	S25E48
29	1998/11/05	22:00	20:58	Halo	360	1124	929	1341	32.5^a	N22W18
30	1998/11/06	03:00	02:18	171	>132	428	386	466	10.0	Backside
31	1998/11/08	11:20	11:18	221	092	579	665	503	-7.2	S22W52
32	1998/11/24	02:30	02:30	Halo	360	1744	1941	1543	-50.0	S30W90*
33	1999/04/24	13:50	13:31	Halo	360	1495	1352	1640	37.1	W90*
34	1999/05/03	05:50	06:06	Halo	360	1584	1511	1658	15.8	N15E32
35	1999/05/27	10:55	11:06	Halo	360	1691	1849	1543	-33.5^a	W90*
36	1999/06/01	18:50	19:37	Halo	360	1772	1767	1777	1.8	NW90*
37	1999/06/04	07:05	07:26	288	>150	2221	2224	2217	-2.0^a	N17W69*
38	1999/06/11	11:45	11:26	Halo	360	1627	1632	1621	-1.1	N38E90*
39	1999/06/22	18:25	18:54	Halo	360	1133	1333	934	-24.7	N22E37
40	1999/06/23	05:50	06:06	Halo	360	450	579	329	-26.7	Backside
41	1999/06/29	19:20	18:54	Halo	360	438	404	472	2.5	S14E01
42	1999/07/05	03:10	02:54	284	190	670	456	898	20.8	SW90*
43	1999/08/28	18:25	18:26	120	>245	462	441	483	1.1	S26W14
44	1999/09/03	03:00	00:06	193	>087	628	586	669	10.3	S35W35

Table 1. (continued)

Number	Radio Date	Time	CME Time	PA	Width	$V1$	$V2_i$	$V2_f$	Accel	Location
45	1999/09/22	13:45	13:54	76	051	1025	1029	1022	-0.4	N17E39
46	1999/10/14	09:10	09:26	Halo	360	1250	1357	1136	-21.2	N11E32
47	1999/10/17	23:27	$00:06^n$	40	>087	247	269	223	-2.7	S20E00
48	1999/11/16	03:27	03:06	81	>098	636	756	510	-9.2	N17E38
49	1999/11/16	05:17	05:30	279	>114	721	517	931	19.8	N18W43
50	2000/01/18	17:31	17:54	Halo	360	759	712	812	5.2	S19E11
51	2000/01/28	20:20	20:12	Halo	360	1177	1226	1126	-9.1	S31W17
52	2000/02/05	19:34	19:54	60	076	632	764	500	-9.7	N26E52
53	2000/02/08	09:05	09:30	Halo	360	1079	1270	874	-35.3	N25E26
54	2000/02/12	03:55	04:31	Halo	360	1107	1171	1047	-8.3	N26W23
55	2000/02/17	20:42	20:06	Halo	360	600	586	614	0.9	S29E07
56	2000/03/07	16:24	16:30	120	108	644	758	530	-10.8	S22E77*
57	2000/03/19	01:00	$23:54^p$	106	>083	1532	1351	1723	37.5	E90*
58	2000/03/27	06:56	07:31	129	090	487	647	347	-9.3	SE90*
59	2000/04/04	15:45	16:32	Halo	360	1188	1142	1232	12.8	N16W66*
60	2000/04/09	23:15	$00:30^n$	Halo	360	383	375	391	1.2	S14W01
61	2000/04/18	15:00	14:54	195	105	668	427	923	23.1	S50W30
62	2000/04/27	14:40	14:30	298	>138	1110	1185	1036	-10.9	N32W90*
63	2000/05/05	15:15	15:50	Halo	360	1594	2023	1213	-103.4	S15W90*
64	2000/05/07	21:15	20:50	245	>098	1781	2111	1466	-71.8	Backside
65	2000/05/15	16:45	16:26	257	>165	1212	1352	1065	-20.5	S24W67*
66	2000/05/22	01:30	01:26	224	>110	737	803	665	-10.2	S20W46
67	2000/06/02	22:00	21:30	69	104	547	473	617	33.2	N16E60*
68	2000/06/06	15:20	15:54	Halo	360	1108	1130	1086	-4.4	N21E13
69	2000/06/10	17:15	17:08	Halo	360	1108	1246	971	-21.2	N22W38
70	2000/06/15	19:52	20:06	298	>116	1081	1174	980	-16.7	N20W65*
71	2000/06/17	03:00	03:28	298	133	857	722	1007	16.4	N22W72*
72	2000/06/19	01:19	$21:30^p$	8	049	459	294	646	12.1	N46E77*
73	2000/06/23	14:40	14:54	293	>103	847	1037	624	-23.3	N26W72*
74	2000/07/10	22:00	21:50	67	>289	1352	1168	1538	35.0	N18E49
75	2000/07/11	04:15	04:50	254	025	345	435	252	-28.1	N13W39
76	2000/07/11	13:00	13:27	Halo	360	1078	1295	850	-42.9	N18E27
77	2000/07/12	20:05	20:30	281	101	820	856	789	-3.2	N17W65*
78	2000/07/14	10:30	10:54	347	360	1674	1815	1534	-96.1^a	N22W07
79	2000/07/22	11:45	11:54	304	>105	1230	1283	1175	-12.4	N14W56
80	2000/09/12	12:00	11:54	Halo	360	1550	1265	1839	58.2	S12W18
81	2000/09/12	18:15	17:30	Halo	360	1053	1174	932	-17.3	NE90*
82	2000/09/16	04:30	05:18	Halo	360	1232	1441	1042	-46.0	N14W07
83	2000/09/19	08:45	08:50	283	076	766	657	880	10.4	N14W46
84	2000/09/21	15:45	16:06	312	029	445	458	432	-1.7	NW90*
85	2000/09/25	02:20	02:50	Halo	360	587	691	475	-25.2	N17W15

Table 1. (continued)

Number	Radio Date	Time	CME Time	PA	Width	$V1$	$V2_i$	$V2_f$	Accel	Location
86	2000/10/16	07:10	07:27	Halo	360	1336	1281	1396	9.9	W90*
87	2000/10/25	09:30	08:26	Halo	360	770	605	948	17.4	W90*
88	2000/11/03	18:35	18:26	Halo	360	291	121	475	16.4	N02W02
89	2000/11/08	23:20	23:06	Halo	360	1345	1195	1488	106.4^a	N10W77*
90	2000/11/12	14:25	14:50	257	050	581	615	545	-5.5	SW90*
91	2000/11/18	20:40	13:54	74	120	553	332	781	16.2	N11E37
92	2000/11/23	08:16	06:06	Halo	360	492	400	595	9.2	S26W40
93	2000/11/23	21:00	20:30	124	>148	1198	1130	1271	12.2	S20E60*
94	2000/11/24	05:10	05:30	Halo	360	1074	1191	942	-18.3	N20W05
95	2000/11/24	15:25	15:30	Halo	360	1245	1269	1219	-3.3	N22W07
96	2000/11/24	22:24	22:06	Halo	360	1005	1012	999	-0.8	N19W16
97	2000/11/25	01:25	01:31	Halo	360	2519	2528	2510	-5.0^a	N07E50
98	2000/11/25	19:00	19:31	Halo	360	671	770	568	-10.8	N20W23
99	2000/11/25	19:55	21:30	345	059	388	161	635	12.4	N20W27
100	2000/11/26	07:35	06:30	286	>227	984	579	1409	54.4	S30W50
101	2000/11/26	17:00	17:06	Halo	360	980	935	1026	5.8	N18W38

PA - Position Angle measured clockwise from Solar North in degrees

$V1-$ 1st order speed in km s^{-1}, $V2_i-$ 2nd order speed in km s^{-1} at first measurement height, $V2_f-$ 2nd order speed in km s^{-1} at final measurement height.

^{p} previous day

^{n} next day

* limb event